# Analysis of Pulsating High-Frequency Injection Self-Sensing Control for CSI PM Motor Drives

Renato Amorim Torres, *Member, IEEE*, Sangwhee Lee, *Member, IEEE*, Hang Dai, *Member, IEEE*, Woongkul Lee, *Member, IEEE*, Thomas M. Jahns, *Life Fellow, IEEE*, and Bulent Sarlioglu, *Fellow, IEEE*

***Abstract*—This article addresses the underexplored field of self-sensing rotor position estimation control methods in current-source inverter (CSI) drives, an increasingly appealing topology due to advancements in monolithic wide bandgap four-quadrant switches. While numerous techniques have been devised for voltage source inverters, the pulsating vector excitation saliency-based method (PVE) emerges as a standout performer in motors with low saliency ratios, such as surface permanent magnet machines. This article guides the adaptation of the PVE method for CSI-based motor drives, emphasizing crucial aspects like addressing resonances, handling potentially unbalanced output filter capacitors, and utilizing even harmonics for permanent magnet flux polarity identification during the method's startup. Additionally, the study delves into a discussion on the benefits and challenges inherent in utilizing CSIs for motor drives, substantiated by experimental results validating the presented analyses.**

***Index Terms*—Current-source inverter, high-frequency injection, pulsating vector excitation, rotor position estimation, self-sensing, sensorless.**

## I. Introduction

SELF-SENSING (or sensorless) rotor position estimation techniques make it possible to eliminate the angular position sensor (such as encoders and resolvers) from motor drives. These methods are attractive for several applications since they reduce the motor drive's overall cost and volume, increase the drive system's reliability, and improve its manufacturability [1].

Self-sensing control can be divided into two major categories: 1) back-electromotive force (EMF) estimation method and 2) high-frequency injection (HFI) method. The back-EMF estimation methods first estimate the back-EMF and extract rotor position using post-processing methods such as the phase-locked loop or observers [2]. However, the back-EMF estimation method cannot provide initial rotor position information and is unsuitable for low-speed operations when the motor's back-EMF is small.

On the other hand, HFI methods rely on the motor's saliency and response to the injected HF signal to extract the rotor position. The HFI methods are well suited for initial rotor position estimation and motors under low-speed operations. The rotating vector excitation method (RVE) is the first type of HFI method. The HF rotating magnetic fields are injected into the stationary reference frame, and the rotor position is extracted from the negative sequence. However, RVE relies on the spatial saliency of the motor, limiting its application to interior permanent magnet (IPM) machines [3]. The pulsating vector excitation method (PVE) injects an HF signal into the estimated rotor reference frame. It relies on the motor's magnetic saliency, making it applicable for IPM and surface mount PM (SPM) machines. Thus, PVE is a self-sensing method that can estimate the rotor position from zero to low-speed operation of SPM motor drives [3].

Despite the extensive self-sensing control techniques reported to date, most are designed for voltage-source inverter (VSI) fed motor drives. Recent advances in the development of wideband gap (WBG) based monolithic four-quadrant switches with reverse voltage blocking capabilities are now offering appealing switch candidates for use in current source inverters (CSIs) [4]. CSIs offer attractive advantages compared to traditional VSIs, such as quasi-sinusoidal output voltage waveforms that significantly reduce the voltage stress on machine windings, resulting in increased reliability, lifetime, and improved machine power density due to thinner winding insulation requirements [5]. Also, WBG-based CSI can have a high switching frequency, leading to low dc-link inductance requirements and fast dynamic response [5].

In contrast to VSIs, CSIs have improved compatibility with low-inductance machines due to the filtering effect output capacitors. Exciting a low-inductance machine with a VSI can lead to excessive phase current ripple and high-frequency (HF) current harmonics, resulting in elevated machine losses and torque ripple [6]. In contrast, the CSI's output capacitors provide additional filtering of the inverter pulsewidth modulation (PWM) switching harmonics, dramatically reducing the machine's stator

Received 11 February 2024; revised 3 July 2024 and 24 September 2024; accepted 27 October 2024. Date of publication 20 November 2024; date of current version 26 December 2024. This work was supported in part by the U.S. Advanced Research Projects Agency-Energy, US Department of Energy, under Grant DE-AR0000893 and in part by the Wisconsin Electric Machines and Power Electronics Consortium, including access to its laboratory facilities. This article was presented at the IEEE International Symposium on Sensorless Control for Electrical Drives, Aug. 16–18, 2023 [DOI: 10.1109/SLED57582.2023.10261387]. Recommended for publication by Associate Editor D. Xu. *(Corresponding author: Sangwhee Lee.)*

Renato Amorim Torres is with the General Motors Research and Development, Pontiac, MI 48341 USA (e-mail: renatoamorimtorres@gmail.com).

Sangwhee Lee, Hang Dai, Thomas M. Jahns, and Bulent Sarlioglu are with the Wisconsin Electric Machines and Power Electronic Consortium, University of Wisconsin–Madison, Madison, WI 53706 USA (e-mail: sangwhee.lee@wisc.edu; hangdai@ieee.org; jahns@engr.wisc.edu; sarlioglu@wisc.edu).

Woongkul Lee is with the Elmore Family School of Electrical and Computer Engineering, Purdue University, West Lafayette, IN 47906 USA (e-mail: wklee@purdue.edu).

Color versions of one or more figures in this article are available at https://doi.org/10.1109/TPEL.2024.3503502.

Digital Object Identifier 10.1109/TPEL.2024.3503502

current ripple even for machines with very low machine inductances [7]. Although the topic is not explored in this article, low machine inductance helps reduce the sensitivity of model-based back-EMF rotor position estimation to the current measurement accuracy [4]. Therefore, the improved compatibility of CSIs with low-inductance machines opens a promising pathway to improved model-based rotor position estimation accuracy compared to VSI-fed motor drives.

The extensive research on self-sensing control techniques reported to date has been primarily focused on their implementation with VSI drives. These works provide little insight into how these techniques perform in CSI-based drives and what modifications are required to obtain the best possible performance. As discussed later, there are noticeable differences between the implementation of self-sensing control techniques due to VSI and CSI's topological differences. Only a few papers have reported investigations of self-sensing control techniques for CSIs [8], [9], [10], [11], [12], [13], [14], [15], [16], [17], [18], [19], [20]. Those works are generally limited to induction machines or thyristor-based drives, severely restricting the motor drive switching frequency and control bandwidth. Additionally, most of these papers do not provide a comprehensive approach that includes practical issues, such as the possibility of unbalanced output filter capacitors.

Among the CSI-based references that investigate self-sensing techniques for synchronous motor drives, most present techniques are suitable for mid- to high-speed range based on back-EMF estimation. To the best of the authors' knowledge, only one reference [17] has been found in the literature investigating the HFI technique to achieve low-speed operation in current-source-fed IPM machine drives. Low-speed HFI self-sensing methods are crucial for ensuring full-range self-sensing operation (from zero to high speed), allowing for the complete elimination of position sensors while maintaining smooth acceleration at startup. Applications that benefit from this technology include traction systems, conveyor systems, and household appliances like washing machines, where precise control and smooth acceleration are essential. Even though [17] lays the foundation for attaining low-speed operation of self-sensing control using current source-fed drives, its focus on silicon-based inverters with low switching frequencies limits its applicability to the new generation of WBG devices-based CSIs. For example, the adoption of thyristor-based inverters in [18] limited the maximum value of the injected signal to a very low value of only 300 Hz.

This article investigates the PVE's application on CSI-fed SPM motor drives (see Fig. 1). Attention mainly focuses on operating at static and low speeds using SPM machines. The rest of this article is organized as follows. Section II provides a detailed explanation of the PVE saliency-based rotor position estimation method in current-source inverters, while Section III presents essential aspects to consider when selecting the frequency of the HF injected signal. Section IV explores the effect of unbalanced output capacitors on the performance of the rotor position estimation. A novel PM flux polarity identification method is proposed in Section V, and Section VI presents experimental results that support the presented analytical results. Finally, Section VII concludes this article.

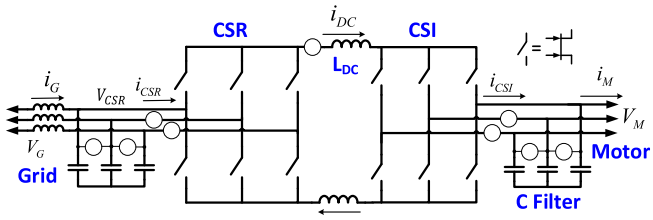


Fig. 1. Schematic of CSI-fed SPM motor drive [23].

## II. Pulsating Vector Excitation Saliency-Based Rotor Position Estimation Methods for CSI-PM Motor Drive

The PVE saliency-based rotor position estimation method used in VSI-based motor drives [3] can be adapted to CSI-based motor drives. However, some topological differences, such as the presence of output filter capacitors, must be considered. This section explains how to tailor the PVE saliency-based method for CSI-based motor drives, investigating and analyzing unique aspects such as capacitor unbalance and CSI-load resonance.

### A. Modeling of PVE for CSI-PM Motor Drives

The set of equations (1) describes the dynamics of a PM synchronous machine and the CSI output filter capacitor in the synchronous reference frame

$$\begin{bmatrix} v_d^e \\ v_q^e \end{bmatrix} = \begin{bmatrix} R_s + L_d p & -\omega_r L_q \\ \omega_r L_d & R_s + L_q p \end{bmatrix} \begin{bmatrix} i_{s,d}^e \\ i_{s,q}^e \end{bmatrix} + \begin{bmatrix} 0 \\ \omega_r \lambda_{\mathrm{PM}} \end{bmatrix}$$
$$p \begin{bmatrix} v_d^e \\ v_q^e \end{bmatrix} = \begin{bmatrix} 0 & \omega_r \\ -\omega_r & 0 \end{bmatrix} \begin{bmatrix} v_d^e \\ v_q^e \end{bmatrix} + \begin{bmatrix} 1/C & 0 \\ 0 & 1/C \end{bmatrix} \begin{bmatrix} i_{c,d}^e \\ i_{c,q}^e \end{bmatrix} \quad (1)$$

where the synchronous reference frame is represented by the superscript $e$. The subscripts $d$ and $q$ represent $d$- and $q$-axis components. Therefore, $v_d^e$, $v_q^e$, $i_{s,d}^e$, $i_{s,q}^e$, $i_{c,d}^e$, $i_{c,q}^e$, $L_d$, and $L_q$ corresponds to the $d$- and $q$-axis components of the machine terminal voltage, stator currents, output capacitors currents, and machine inductance. The resistance $R_s$ corresponds to the machine stator resistance, $C$ is CSI output filter capacitance, $\omega_r$ is the electrical angular speed of the rotor, $\lambda_{\mathrm{PM}}$ is the PM flux linkage, and $p$ is the derivative operator. It is assumed that the CSI output capacitors are balanced for these equations.

Assuming that the injected signal frequency is high and the machine is operating at a low speed, the speed-dependent terms in (1) can be neglected. As a result, (1) simplifies to

$$\begin{bmatrix} \tilde{\boldsymbol{V}}_{dh}^e \\ \tilde{\boldsymbol{V}}_{qh}^e \end{bmatrix} = \begin{bmatrix} \boldsymbol{Z}_{dh} & 0 \\ 0 & \boldsymbol{Z}_{qh} \end{bmatrix} \begin{bmatrix} \tilde{\boldsymbol{I}}_{dh}^e \\ \tilde{\boldsymbol{I}}_{qh}^e \end{bmatrix}$$
$$\boldsymbol{Z}_{dh} = \frac{R_{sh} + j\omega_h L_{dh}}{1 + j\omega_h R_{sh} C_h - \omega_h^2 L_{dh} C_h}$$
$$\boldsymbol{Z}_{qh} = \frac{R_{sh} + j\omega_h L_{qh}}{1 + j\omega_h R_{sh} C_h - \omega_h^2 L_{qh} C_h} \quad (2)$$

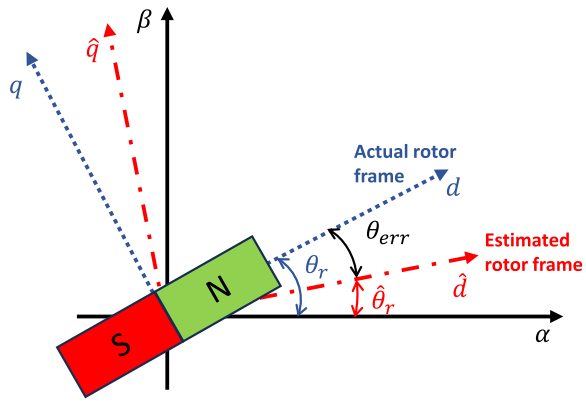


Fig. 2. Vector representation of the pulsating vector excitation method error angle $\boldsymbol{\theta_{err}}$ between the actual rotor position $\boldsymbol{\theta_r}$ and the estimated rotor position $\widehat{\boldsymbol{\theta_r}}$.

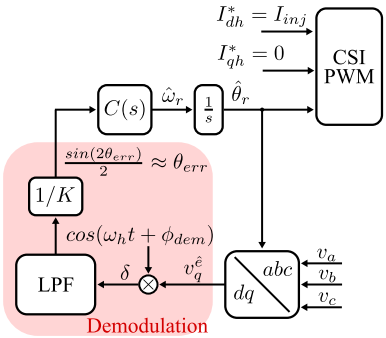


Fig. 3. Control block diagram of a closed-loop system for a PVE scheme for rotor angle self-sensing that minimizes angle error $\theta_{err}$ between real rotor position $\theta_r$ and estimated rotor position $\hat{\theta}_r$.

where the subscript $h$ refers to the HF components and steady-state operation is assumed (i.e., $p = j\omega_h$). Note that the voltage and current variables in (2) are phasors and denoted using capitalized bold variable names with a tilde accent (e.g., $\tilde{\boldsymbol{X}} = a + jb$). The impedances are complex numbers denoted using uppercase bold variable names (e.g., $\boldsymbol{X} = a + jb$). The conversion from the phasors to the steady-state time domain is given by $x\,(t) = Re\{\tilde{\boldsymbol{X}} e^{j\omega_h t}\}$.

The voltage and current phasors of (2) can be translated to the estimated synchronous reference frame (superscript $\hat{e}$) using the relation operator $\boldsymbol{x}^e = T(\theta)\boldsymbol{x}^{\hat{e}}$, given by

$$T\ (\theta) = \begin{bmatrix} \cos(\theta) & \sin(\theta) \\ -\sin(\theta) & \cos(\theta) \end{bmatrix} \tag{3}$$

and the error angle is defined as

$$\theta_{err} \triangleq \theta_r - \widehat{\theta_r} \tag{4}$$

where $\theta_r$ is the actual rotor position and $\widehat{\theta_r}$ is the estimated rotor position $\widehat{\theta_r}$ both in electrical angle, as shown in Fig. 2. Applying $\theta_{err}$ to the voltages and currents in (2) leads to

$$\begin{bmatrix} \tilde{\boldsymbol{V}}^{\hat{e}}_{dh} \\ \tilde{\boldsymbol{V}}^{\hat{e}}_{qh} \end{bmatrix} = T^{-1}\ (\theta_{err}) \begin{bmatrix} \boldsymbol{Z}_{dh} & 0 \\ 0 & \boldsymbol{Z}_{qh} \end{bmatrix} T\,(\theta_{err}) \begin{bmatrix} \tilde{\boldsymbol{I}}^{\hat{e}}_{dh} \\ \tilde{\boldsymbol{I}}^{\hat{e}}_{qh} \end{bmatrix} \tag{5}$$

which is the HF machine model in the estimated synchronous reference frame. This machine model can be re-expressed as

$$\begin{bmatrix} \tilde{\boldsymbol{V}}^{\hat{e}}_{dh} \\ \tilde{\boldsymbol{V}}^{\hat{e}}_{qh} \end{bmatrix} = \begin{bmatrix} a_{11} & a_{12} \\ a_{21} & a_{22} \end{bmatrix} \begin{bmatrix} \tilde{\boldsymbol{I}}^{\hat{e}}_{dh} \\ \tilde{\boldsymbol{I}}^{\hat{e}}_{qh} \end{bmatrix}$$

$$\begin{aligned} a_{11} &= \boldsymbol{Z}_{avg} - \boldsymbol{Z}_{diff}\cos(2\theta_{err}) \\ a_{12} &= -\boldsymbol{Z}_{diff}\sin(2\theta_{err}) \\ a_{21} &= -\boldsymbol{Z}_{diff}\sin(2\theta_{err}) \\ a_{22} &= \boldsymbol{Z}_{avg} + \boldsymbol{Z}_{diff}\cos(2\theta_{err}) \\ \boldsymbol{Z}_{avg} &= (\boldsymbol{Z}_{dh} + \boldsymbol{Z}_{qh})/2 \boldsymbol{Z}_{diff} = (\boldsymbol{Z}_{qh} - \boldsymbol{Z}_{dh})/2. \end{aligned} \tag{6}$$

If the HF injected current is only applied in the $d$-axis, as shown in

$$\begin{aligned} i^{\hat{e}}_{dh} &= I_{inj}\cos(\omega_h t) \rightarrow \tilde{\boldsymbol{I}}^{\hat{e}}_{dh} = I_{inj} \\ i^{\hat{e}}_{qh} &= 0 \rightarrow \tilde{\boldsymbol{I}}^{\hat{e}}_{qh} = 0. \end{aligned} \tag{7}$$

The simplified HF $d$- and $q$-axis voltages can be obtained from (6), as shown in

$$\begin{aligned} \tilde{\boldsymbol{V}}^{\hat{e}}_{dh} &= I_{inj}\ (\boldsymbol{Z}_{avg} - \boldsymbol{Z}_{diff}\cos(2\theta_{err})) \\ \tilde{\boldsymbol{V}}^{\hat{e}}_{qh} &= I_{inj}\ (-\boldsymbol{Z}_{diff}\sin(2\theta_{err}))\,. \end{aligned} \tag{8}$$

Notice from (8) that the $q$-axis voltage component in the estimated reference frame $\tilde{\boldsymbol{V}}^{\hat{e}}_{qh}$ is zero when the rotor position error $\theta_{err}$ is zero. Therefore, a control loop can be designed to minimize $\theta_{err}$, where the feedback is based on the measured $q$-axis voltage $v^{\hat{e}}_{qh}$.

### *B. PVE Control Loop Strategy for CSI-PM Motor Drives*

The control loop is shown in Fig. 3, where the demodulation concept is used in the red dashed-line box. Let us assume that the signal $v^{\hat{e}}_q$ has a HF quadrature voltage component in the format $v^{\hat{e}}_{qh} = A\cos(\omega_h t + \phi_{hq})$. By multiplying $v^{\hat{e}}_{qh}$ by a HF demodulating cosine wave $\cos(\omega_h t + \phi_{dem})$, the signal $\delta$ (identified in the block diagram of Fig. 3) is generated. The signal $\delta$ has two components: a dc component and a HF component, as shown in

$$\begin{aligned} \delta &= v^{\hat{e}}_{qh} \cdot \cos(\omega_h t + \phi_{dem}) \\ &= A\cos(\omega_h t + \phi_{hq}) \cdot \cos(\omega_h t + \phi_{dem}) \\ &= A\left(\frac{\cos(\phi_{hq} - \phi_{dem})}{2} + \frac{\cos(2\omega_h t + \phi_{hq} + \phi_{dem})}{2}\right). \end{aligned} \tag{9}$$

The HF component will be filtered out using the low-pass filter (identified as an LPF in the block diagram of Fig. 3), and the remaining dc component will be used to extract the position estimation. Therefore, maximizing the dc-component improves the signal-to-noise ratio (SNR). From (9), it can be seen that, for a fixed signal amplitude A, the dc-component is maximized when $\phi_{dem} = \phi_{hq}$ .

From (8), the signal $v_{qh}^{\hat{e}}$ can be represented by a phasor of magnitude A and phase $\phi_{hq}$ (i.e.,$\tilde{\boldsymbol{V}}_{qh}^{\hat{e}} \triangleq A\angle\phi_{hq}$), where $A = -I_{inj} \cdot |\boldsymbol{Z}_{diff}| \cdot \sin 2\theta_{err}$ and $\phi_{hq} = \angle \boldsymbol{Z}_{diff}$. Using (9) and setting the phase of the demodulating cosine wave to $\phi_{dem} = \phi_{hq}$ yields

$$\delta = \frac{A}{2} + \frac{\cos\left(2\omega_h t + 2\theta_{hq}\right)}{2} \tag{10}$$

$$A = -I_{inj} \cdot |\boldsymbol{Z}_{diff}| \cdot \sin\left(2\theta_{err}\right) \text{ and } \phi_{hq} = \angle \boldsymbol{Z}_{diff}.$$

By applying a low-pass filter to the signal $\delta$, (11) is obtained

$$\text{LPF}\ \{\delta\} = \frac{A}{2} = -|\boldsymbol{Z}_{diff}|\, I_{inj} \frac{\sin\left(2\theta_{err}\right)}{2}. \tag{11}$$

Once the position estimator converges and is tracking the actual rotor position, it can be assumed that $\boldsymbol{\theta_{err}}$ is approximately zero; therefore, $\mathbf{sin}(2\boldsymbol{\theta_{err}}) \approx 2\boldsymbol{\theta_{err}}$. Thus, the estimated rotor position angle error $\boldsymbol{\theta_{err}}$ can be estimated by dividing the result of (11) by the constant $\boldsymbol{K}$, as shown in (12). Such operation is identified as $\mathbf{1}/\boldsymbol{K}$ in the block diagram of Fig. 3

$$\frac{\text{LPF}\,\{\delta\}}{K} \approx \theta_{err}, \text{ where } K = -|\boldsymbol{Z}_{diff}|\, I_{inj}. \tag{12}$$

The final step of the control loop involves correcting the estimated rotor position $\widehat{\theta_r}$ based on the rotor position estimation error $\theta_{err}$ that is extracted using the demodulating process mentioned above. This correction can be implemented using various controllers, such as a PI controller. To keep it generic, the controller is identified in Fig. 3 as $C(s)$. The output of the controller is the angular speed $\hat{\omega}_r$ of the estimated rotor reference frame. Finally, the estimated rotor position $\widehat{\theta_r}$ is obtained by integrating the estimated reference frame angular speed $\hat{\omega}_r$. The estimated rotor position is then used by the PWM modulation block and the Park transformation.

A critical observation must be made. As mentioned before, the demodulation cosine waveform's phase angle $\phi_{dem}$ should be equal to $\phi_{hq}$ to maximize the dc component of signal $\delta$, which is ultimately used for extracting the rotor position estimation error. The angle $\phi_{hq}$ corresponds to the angle of the impedance difference between the $d$- and $q$-axis ($\phi_{hq} = \angle \boldsymbol{Z}_{diff}$). As will be shown in Section III, the closer the frequency of the injected signal is to the $d$- or $q$-axis resonant frequencies, the higher the impedance difference $\boldsymbol{Z}_{diff}$. Since a higher impedance difference improves the SNR of the estimated rotor position, injecting signals with frequencies close to the resonance can be advantageous. However, the angle of the impedance difference also changes quickly as the injected signal frequency approaches one of the resonant frequencies; thus, it is essential to correct the phase of the demodulating cosine wave by setting $\phi_{dem} = \phi_{hq}$ to extract the maximum benefit of injecting signals close to the resonant frequencies. This aspect has not been previously reported in the literature.

TABLE I
CSI-SPM MOTOR DRIVE SYSTEM PARAMETERS

| Parameters | Symbol | Value |
|---|---|---|
| Output filter phase capacitance ($\mu$F) | $C$ | 2.2 |
| Machine high-freq. d-axis inductance (mH) | $L_{dh}$ | 3.65 |
| Machine high-freq. q-axis inductance (mH) | $L_{qh}$ | 4.07 |
| Saliency ratio | $L_{qh}/L_{dh}$ | 1.115 |
| Machine phase resistance ($\Omega$) | $R_s$ | 0.1575 |
| Machine pole pairs | $P$ | 4 |
| Torque constant (Nm/Arms) | $K_t$ | 1.93 |
| Maximum torque current (Arms) | $I_{MAX}$ | 8.5 |
| Total system inertia (Kg m$^2$) | $I$ | 0.04 |
| Permanent magnet flux linkage (V·s) | $\lambda_{PM}$ | 0.2515 |
| Switching/Sampling frequency (kHz) | $f_s$ | 70 |
| Voltage sensor analog filter cutoff freq. (kHz) | $f_{c,v}$ | 30 |
| Current sensor analog filter cutoff freq. (kHz) | $f_{c,i}$ | 30 |

## III. FREQUENCY SELECTION OF HIGH-FREQUENCY INJECTED SIGNAL FOR PVE OF CSI-FED MOTOR DRIVE

Table I shows the CSI-SPM motor drive parameters used throughout the subsequent analysis. Different factors must be considered when selecting the frequency of the injected signal, such as losses, SNR ratio, modulation index allocation, bandwidth, and distortions due to unbalanced output capacitors. The combination of the output capacitor and the machine inductances creates resonant circuits. Care must be taken to prevent the HF injected signal from heavily exciting these resonant frequencies, which would induce high currents in the machine and output capacitors, potentially damaging the drive due to excessive losses or overvoltage. Nevertheless, injecting the HF signal at a frequency close to the resonant frequency can be advantageous. The first advantage is the amplification of the HF injected signal [21], where a minimal current injected by the CSI can drive large currents and voltages across the CSI output capacitors and machine terminals. This property enables allocating a small portion of the CSI dc-link current towards the HFI. Even the amplification gain can be regulated in real time by modifying the frequency of the injected signal.

It can be seen from (10) that the signal $\delta$, which is ultimately used for extracting the rotor position estimation, is proportional to the magnitude of the impedance difference between the $d$- and $q$-axis $|\boldsymbol{Z}_{diff}|$. Therefore, a higher $|\boldsymbol{Z}_{diff}|$ improves the SNR of the estimated rotor position. Fig. 4 shows the value of $|\boldsymbol{Z}_{diff}|$ in the CSI system investigated for different frequencies in logarithmic scale, where a magnified version of $|\boldsymbol{Z}_{diff}|$ is also shown in red box. Notice that this value peaks at either the $d$-axis or $q$-axis resonant frequencies (1776 Hz and 1682 Hz, respectively, as shown in Fig. 4).

From Fig. 4, it is evident that the impedance difference $|\boldsymbol{Z}_{diff}|$ drops sharply for frequencies away from the resonant points. For frequencies lower than the resonant frequencies, $|\boldsymbol{Z}_{diff}|$ exhibits a 20 dB/dec slope, whereas for frequencies higher than the resonant points, it follows a $-60$ dB/dec slope. This behavior highlights a critical point: if the HFI is either too low or too high, a significant current will be required from the CSI to produce a small voltage response, which, as mentioned earlier, is used to determine rotor position. This phenomenon can

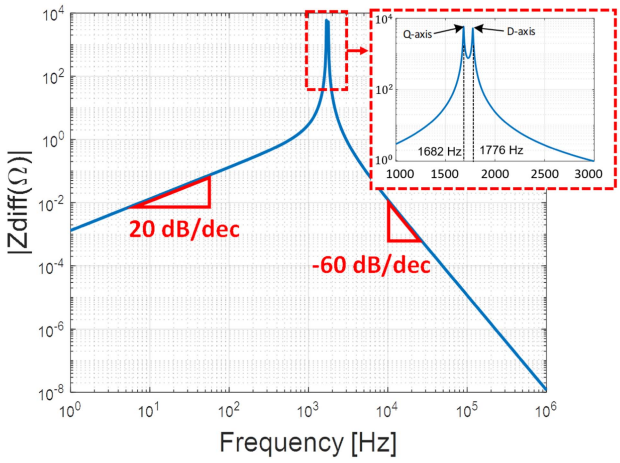


Fig. 4. Calculated magnitude of the impedance difference between the $d$- and $q$-axes ($\boldsymbol{Z}_{diff}$) plotted as a function of the frequency of the injected signal. Red box: magnified $\boldsymbol{Z}_{diff}$ for short range with linear horizontal scale.

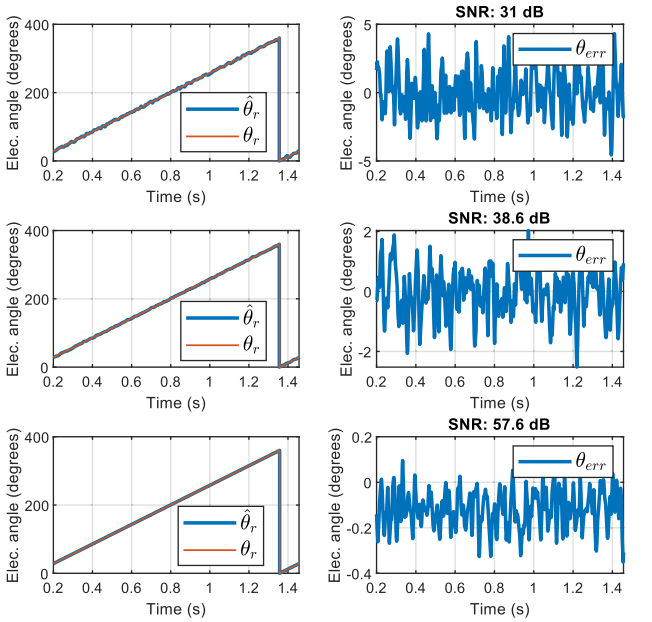


Fig. 5. Simulation results comparing the SNR ratio of the rotor position estimation for different injected signal frequencies: (top) 700 Hz; (middle) 1000 Hz; and (bottom) 1500 Hz.

pose a potential drawback in the PVE of CSI-fed motor drives, particularly since frequencies up to tens of kHz are often within the audible range depending on the application.

One potential solution is to reduce the output filter capacitance, which would raise the resonant frequency and allow for higher frequencies of the injected signal. This reduction has additional implications on CSI control performance. For instance, lowering the output filter capacitance decreases the phase delay introduced by the output filter capacitor at the CSI's fundamental frequency, which turns out to be an advantage. However, On the downside, a smaller output filter capacitance may reduce the system's ability to absorb energy during transients or fault conditions. A comprehensive analysis of the impact of the resonant circuit on the CSI frequency response and control performance, including the effects of varying output filter capacitance on phase delay, can be found in [22].

Fig. 5 shows simulation results comparing the SNR ratio of the rotor position estimation for different injected signal frequencies, namely 700 Hz, 1000 Hz, and 1500 Hz. The simulation included different aspects of the power electronics, such as voltage drop across switching devices, overlap time, and sensor dynamics. A voltage-behind reactance salient PM machine model is used in a torque-mode operation. Magnetic saturation effects were disregarded. Band-limited white noise was injected into the voltage and current signals to evaluate the SNR of the rotor position estimation.

The SNR was calculated using

$$\begin{aligned}\mathrm{SNR}_{dB} &= 10\log_{10}\left(\frac{P_{\text{signal}}}{P_{\text{noise}}}\right)\\ &= 10\log_{10}\left(\frac{\mathrm{RMS}_{\text{signal}}}{\mathrm{RMS}_{\text{noise}}}\right)^2. \end{aligned} \tag{13}$$

It should be noted that the estimated rotor position is converted into a sinusoidal signal as $\sin(\hat{\theta}_{est})$ to evaluate the SNR using (13). The simulation results confirm that operation closer to the resonant frequency improves the SNR. For example, when injecting the signal at 1500 Hz, the SNR value is 26.6 dB higher than an injection at 700 Hz. This result is somewhat expected since the HF voltage signal response amplitude, used for extracting the rotor position information, increases at frequencies closer to the resonant frequencies.

## IV. Effects of Unbalanced CSI Output Capacitors

Although the CSI enables amplification of the injected signal by leveraging the resonant circuit, the presence of the output filter capacitors can introduce undesirable disturbances that must be better understood. This section investigates the perturbation on the rotor position estimation by a potential unbalance of the CSI's output filter capacitors and the resulting sensitivity of the rotor position estimation accuracy to such unbalances.

In the preceding section, the impedance matrix terms $Z_{12}$ and $Z_{21}$ in (2) are zero. These null terms are a consequence of a three-phase balanced system with no cross-coupling between the $d$- and $q$-axes of the machine. Li et al. [23] investigated the effect of cross-coupled magnetic saturation on the performance of a saliency-based rotor position estimation method. They reported that the terms $Z_{12}$ and $Z_{21}$ become nonzero ($Z_{12} = Z_{21} \neq 0$) as a result of cross-coupled magnetic saturation. A similar effect occurs in the presence of unbalanced output capacitors; however, in this case, the cross-coupling terms are not constant and vary with the rotor position.

Fig. 6(a) shows the values of the impedances $\boldsymbol{Z}_{dh}$, $\boldsymbol{Z}_{qh}$, and $\boldsymbol{Z}_{dqh}$ for the drive under investigation at different rotor positions (from 0° to 360° electrical), assuming balanced output capacitors. The results show that the three impedances are constant and $\boldsymbol{Z}_{dqh}$ is zero for balanced conditions. Fig. 6(b) and

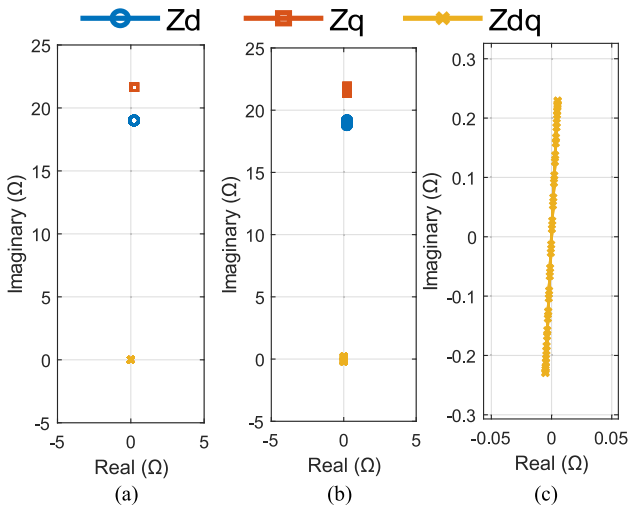


Fig. 6. Calculated load impedances $\boldsymbol{Z_{dh}}$, $\boldsymbol{Z_{qh}}$, and $\boldsymbol{Z_{dqh}}$ of the investigated CSI motor drive for different rotor positions (from 0° to 360° electrical) assuming. (a) Balanced output capacitors. (b) Unbalanced output capacitors ($C_a = 1.1C,\ C_b = C,\ C_c = 0.9C$). (c) Zoomed plot of (b) around the origin.

(c) shows the same plot for unbalanced output capacitors with ±10% errors (i.e., $C_a = 1.1C,\ C_b = C,\ C_c = 0.9C$). In this case, $\boldsymbol{Z}_{dh}$, $\boldsymbol{Z}_{qh}$, and $\boldsymbol{Z}_{dqh}$ are no longer constant and $\boldsymbol{Z}_{dqh}$ takes on nonzero values. See the appendix for a detailed explanation of how to compute the $\boldsymbol{Z}_{dh}$, $\boldsymbol{Z}_{qh}$, and $\boldsymbol{Z}_{dqh}$ terms. Equation (14) (shown at the bottom of the next page) shows the results of applying the same procedure used to derive (3) except that the cross-coupling impedance terms (i.e., $Z_{12} = Z_{21} = \boldsymbol{Z}_{dqh}$ ) are now nonzero. It should be noted in the last equation of (14) that the OFF-diagonal terms now have an additional component of $\boldsymbol{Z}_{dqh}\cos(2\theta_{err})$, which was not present in (5). This component represents a disturbance input for the saliency-based self-sensing algorithm.

Since the PVE strategy is unmodified, (9) remains valid, and the signal $v^{\hat{e}}_{qh}$ can still be represented by a phasor of magnitude $A$ and phase angle $\phi_{hq}$ (i.e., $\tilde{\boldsymbol{V}}^{\hat{e}}_{qh} \triangleq A\angle\phi_{hq}$). However, the amplitude and phase of $v^{\hat{e}}_{qh}$ are now given by: $A = I_{inj}\cdot|\boldsymbol{Z}_{dqh}\cos(2\theta_{err}) - \boldsymbol{Z}_{diff}\sin(2\theta_{err})|$ and $\phi_{hq} = \angle(\boldsymbol{Z}_{dqh}\cos(2\theta_{err}) - \boldsymbol{Z}_{diff}\sin(2\theta_{err}))$. The injected signals are the same as for the balanced capacitance case; $\tilde{\boldsymbol{I}}^{\hat{e}}_{dh} = I_{inj}$ and $\tilde{\boldsymbol{I}}^{\hat{e}}_{qh} = 0$.

As shown in the preceding section, the PVE self-sensing algorithm is designed to regulate the estimated rotor position $\hat{\theta}_r$ by using a feedback loop to drive $\tilde{\boldsymbol{V}}^{\hat{e}}_{qh}$ to zero. In an ideally balanced system, this is achieved when the cross-coupling term $-\boldsymbol{Z}_{diff}\sin(2\theta_{err})$ in (5) equals zero, which translates into $\theta_{err}$ being zero. However, in (14), the cross-coupling term is $\boldsymbol{Z}_{dqh}\cos(2\theta_{err}) - \boldsymbol{Z}_{diff}\sin(2\theta_{err})$, and no angle $\theta_{err}$ satisfies the identity $\boldsymbol{Z}_{dqh}\cos(2\theta_{err}) - \boldsymbol{Z}_{diff}\ \sin(2\theta_{err}) = 0$ since $\boldsymbol{Z}_{dqh}$ and $\boldsymbol{Z}_{diff}$ are not collinear complex numbers. Nevertheless, the PVE control loop will do its best to continuously minimize $\tilde{\boldsymbol{V}}^{\hat{e}}_{qh}$ despite the unbalance

Fig. 7 shows the value of $|\tilde{\boldsymbol{V}}^{\hat{e}}_{qh}|$ calculated via (14) for different estimated rotor position values $\hat{\theta}_r$ when the rotor is static at $\theta_r = 0$. The results show that the minimal value of $|\tilde{\boldsymbol{V}}^{\hat{e}}_{qh}|$ occurs when $\hat{\theta}_r = 3.19°$ (i.e., $\theta_{err} = -3.19°$). This angle corresponds to the same rotor position estimation angle obtained via simulation of the PVE self-sensing algorithm under the same unbalanced capacitor conditions.

As noted previously and shown in Fig. 6(b) and (c), the complex value of $\boldsymbol{Z}_{dqh}$ varies for different rotor positions. This complex value of $\boldsymbol{Z}_{dqh}$ completes two full cycles within a single full rotor electrical cycle (i.e., twice the fundamental excitation frequency). Therefore, the estimation error $\theta_{err}$ is also expected to vary for different rotor positions at twice the fundamental excitation frequency and to be correlated to the magnitude of $\boldsymbol{Z}_{dqh}$. Fig. 8(a) shows the calculated value of $|\boldsymbol{Z}_{dqh}|$ for different rotor positions, while Fig. 8(b) shows the simulation results of the PVE self-sensing algorithm for unbalanced output capacitors. By comparing Fig. 8(a) and (b), the strong correlation between $|\boldsymbol{Z}_{dqh}|$ and $\theta_{err}$ is clearly visible. It is important to mention that since Fig. 8(a) and (b) plot the amplitude of $\boldsymbol{Z}_{dqh}$ and $\theta_{err}$ (without the corresponding phase) it may lead to a wrong impression that $\boldsymbol{Z}_{dqh}$ completes four full cycles (instead of two) within a single full rotor electrical cycle.

Note that increasing the injected signal frequency reduces the impedance of the output filter capacitors while increasing the impedance of the machine inductance, bringing it closer to the resonant frequency. Fig. 9(a) clearly shows that as the injected frequency approaches the resonant frequencies (1682 Hz and 1776 Hz), the magnitude of $\boldsymbol{Z}_{dqh}$ rapidly increases. Once the injected frequency exceeds the resonant frequencies, the magnitude of $\boldsymbol{Z}_{dqh}$ begins to decrease. Additionally, as expected, Fig. 9(b) shows that greater output filter capacitance unbalance results in a larger magnitude of $\boldsymbol{Z}_{dqh}$.

Fig. 10 shows the simulation results of the PVE self-sensing method with unbalanced output ($C_a = 1.1\,C,\ C_b = C,\ C_c = 0.9\ C$) at three different injected signal frequencies: 700 Hz, 1000 Hz, and 1350 Hz. The fundamental frequency is 26.66 Hz, corresponding to 400 r/min and the torque. The results reveal that the rotor position estimation error oscillations grow in amplitude and become unstable as the injected signal frequency nears the first resonant frequency. Additionally, increased rotor position estimation error oscillations lead to more pronounced torque oscillations and noticeable effects on the current and voltage waveforms. Finally, as the injected signal frequency approaches the resonant frequencies, the required voltage response amplitude increases. This is expected because the impedance of the load (comprising the filter capacitance and machine reactance) peaks at the resonant frequencies, necessitating larger voltages to maintain the same current injection.

## V. Permanent Magnet Flux Polarity Identification

Saliency-based self-sensing methods cannot discriminate whether the $d$-axis of the estimated reference frame is aligned with the PM's north pole or south pole. This can be noticed from (11), where two values for $\theta_{err}$ can satisfy the equation

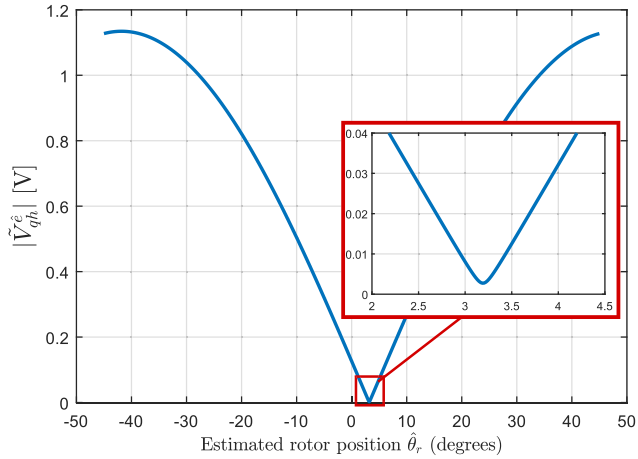


Fig. 7. Value of $|\tilde{\boldsymbol{V}}^{\hat{\boldsymbol{e}}}_{\boldsymbol{qh}}|$ for the investigated CSI drive calculated using (14) for different rotor position estimation values $\hat{\theta}_r$ when the rotor is static at $\theta_r = 0$.

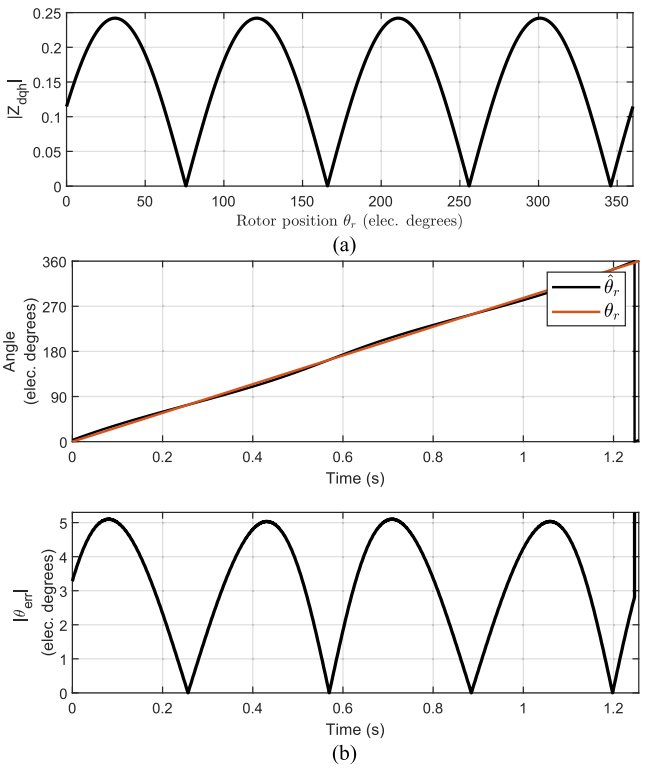


Fig. 8. (a) Calculated $|\boldsymbol{Z}_{\boldsymbol{dqh}}|$ plotted versus rotor position in the presence of unbalanced output capacitors. (b) Simulation results of the PVE self-sensing method for unbalanced output capacitors plotted versus time for one full electrical cycle.

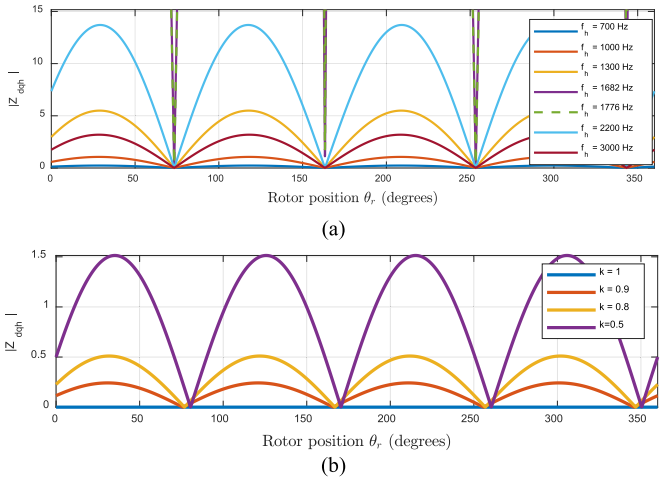


Fig. 9. (a) Calculated $|\boldsymbol{Z}_{\boldsymbol{dqh}}|$ plotted versus rotor position for different values of (a) frequency of injected signal ($f_h$); and (b) for different ratios of capacitor unbalance $k$, where $C_a = kC$, $C_b = C$, $C_c = C/k$.

for a given value of LPF$\{\delta\}$. For example, both $\theta_{err} = 0$ or $\theta_{err} = 180^o$ leads to LPF $\{\delta\} = 0$. The estimated reference frame alignment identification can be achieved using the effect of magnetic saturation. Using magnetic saturation for the PM flux polarity identification in VSIs was discussed in [25]. However, to the best of the authors' knowledge, there is no work on flux polarity identification for CSIs. Therefore, the authors have proposed a method for PM flux polarity identification in CSIs, which relies on the analysis of the odd harmonics present in the voltage response to the current HFI. The proposed method differs from the traditional method used in VSIs, where PM flux polarity identification is done by comparing the peak value of the positive current against the negative peak value of the negative current in response to the voltage HFI.

The following section explains the proposed PM flux polarity identification tailored for CSI-fed drives compared to the method used for VSI-fed drives,

### *A. Proposed Strategy for PM Flux Polarity Identification in CSI-Based Drives*

Suppose that the rotor is aligned, as shown in point A of Fig. 11, where a positive armature current produces a magnetomotive force (MMF) that sums up to the MMF of the PM flux, and a negative current produces an MMF that is subtracted from the PM flux. Then, if a symmetric ac voltage waveform is applied, the amplitude of the positive current will be larger than that of the negative current due to magnetic saturation. Therefore, based on the amplitude of the HF response current, it

$$\begin{bmatrix} \tilde{\boldsymbol{V}}^{\hat{e}}_{dh} \\ \tilde{\boldsymbol{V}}^{\hat{e}}_{qh} \end{bmatrix} = T^{-1}(\theta_{err}) \begin{bmatrix} \boldsymbol{Z}_{dh} & \boldsymbol{Z}_{dqh} \\ \boldsymbol{Z}_{dqh} & \boldsymbol{Z}_{qh} \end{bmatrix} T(\theta_{err}) \begin{bmatrix} \tilde{\boldsymbol{I}}^{\hat{e}}_{dh} \\ \tilde{\boldsymbol{I}}^{\hat{e}}_{qh} \end{bmatrix}$$

$$= \begin{bmatrix} \boldsymbol{Z}_{avg} - \boldsymbol{Z}_{diff}\cos(2\theta_{err}) & \boldsymbol{Z}_{dqh}\cos(2\theta_{err}) - \boldsymbol{Z}_{diff}\sin(2\theta_{err}) \\ \boldsymbol{Z}_{dqh}\cos(2\theta_{err}) - \boldsymbol{Z}_{diff}\sin(2\theta_{err}) & \boldsymbol{Z}_{avg} + \boldsymbol{Z}_{diff}\cos(2\theta_{err}) \end{bmatrix} \begin{bmatrix} \tilde{\boldsymbol{I}}^{\hat{e}}_{dh} \\ \tilde{\boldsymbol{I}}^{\hat{e}}_{qh} \end{bmatrix}. \quad (14)$$

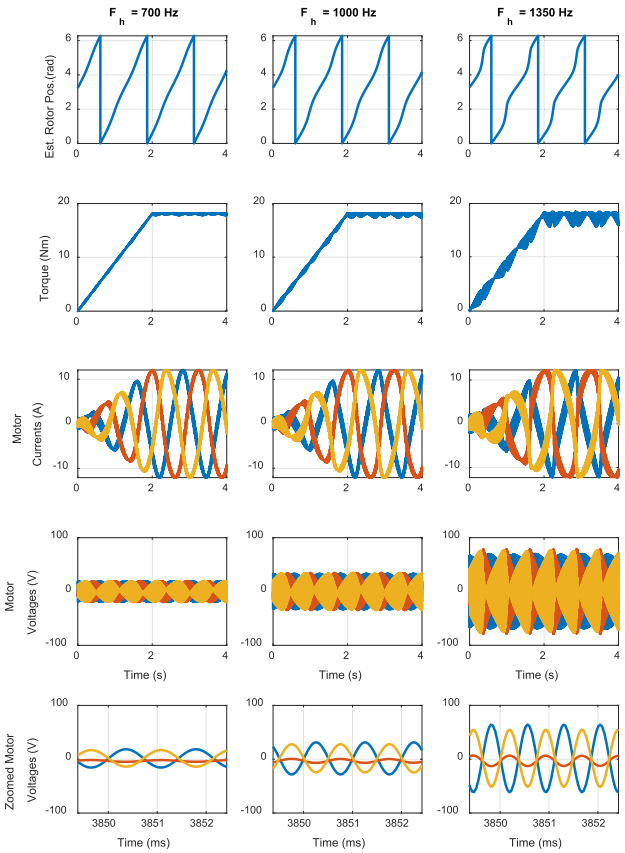


Fig. 10. Simulations of the PVE self-sensing method assuming unbalanced output capacitors ($C_a = 1.1C,\ C_b = C,\ C_c = 0.9C$) for different injected signal frequencies (i.e., 700, 1000, and 1350 Hz) at 26.66 Hz electrical excitation frequency (400 r/min).

is possible to define whether the $d$-axis of the estimated reference frame is correctly aligned with the PM flux or requires a rotation of 180°. The effect of magnetic saturation can also be used for PM flux polarity identification in CSI-based drives; however, there are some practical differences, as highlighted next.

Consider a nonideal machine (i.e., susceptible to magnetic saturation) at zero speed with its stator excited by an ideal VSI injecting a pulsating HF sinusoidal voltage in the $d$-axis of the estimated reference frame ($v^{\hat{e}}_{dh} = v_{inj}\cos(\omega_h t)$). Fig. 12(a) shows the injected voltage at the $d$-axis of the estimated reference frame (blue trace) and the measured current responses (orange traces) in the same reference frame for two conditions: 1) $d$-axis reference frame correctly aligned and 2) $d$-axis reference frame misaligned by 180°.

On the other hand, Fig. 12(b) shows similar injection and response signals, but now the machine is excited by an ideal CSI (with output filter capacitors) injecting an HF sinusoidal current in the $d$-axis of the estimated reference frame ($i^{\hat{e}}_{dh} = I_{inj}\cos(\omega_h t)$). Note that the responses are now voltage signals. The voltage response signals (orange traces) are also measured in the estimated $d$-axis reference frame of the machine for the same two conditions of Fig 12(a): 1) the $d$-axis reference frame correctly aligned and 2) the $d$-axis reference frame misaligned by 180°.

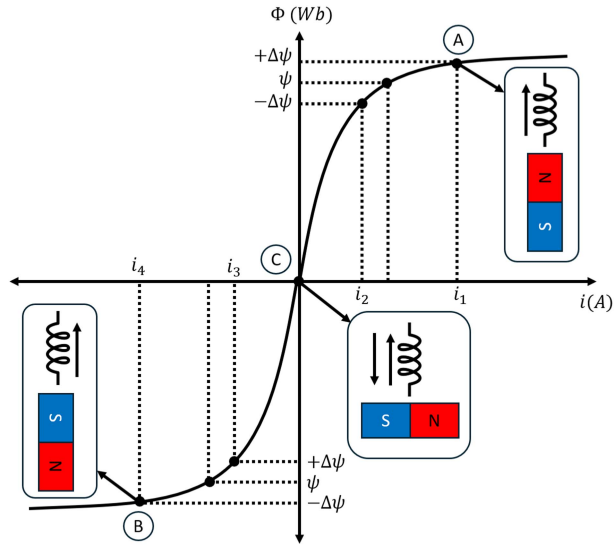


Fig. 11. Effect of magnetic saturation for different rotor positions.

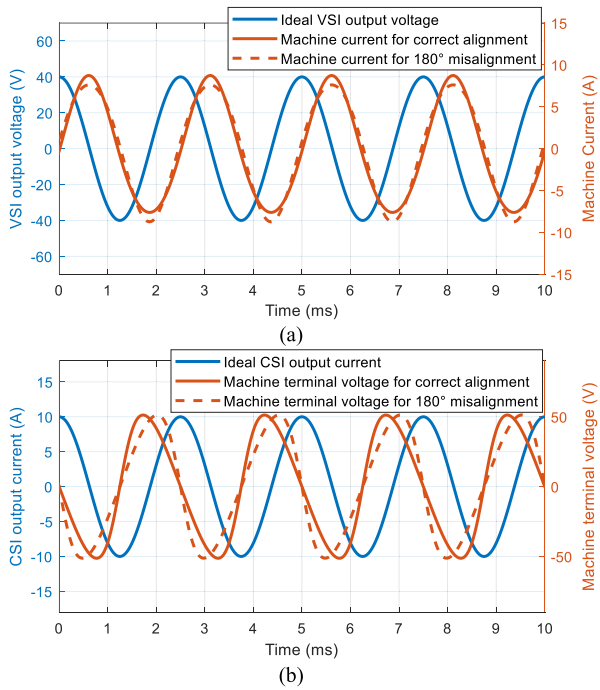


Fig. 12. D-axis currents and terminal voltages for a machine at zero speed excited by. (a) Ideal VSI injecting sinusoidal voltage in the $d$-axis of the estimated reference frame. (b) Ideal CSI injecting sinusoidal current in the d-axis of the estimated reference frame. Wave-forms plotted for two scenarios: (i) Estimated reference frame is correctly aligned with the PM (blue); (ii) estimated reference frame is 180° misaligned (orange).

From Fig. 12(a), one can verify that when the machine is excited with a VSI, the PM flux polarity identification can be done by comparing the peak value of the positive current against the negative peak value of the negative current, as previously explained. By duality, one may expect that, in the case of the CSI-driven system, the polarity identification could be done by comparing the peak values of the positive and negative terminal

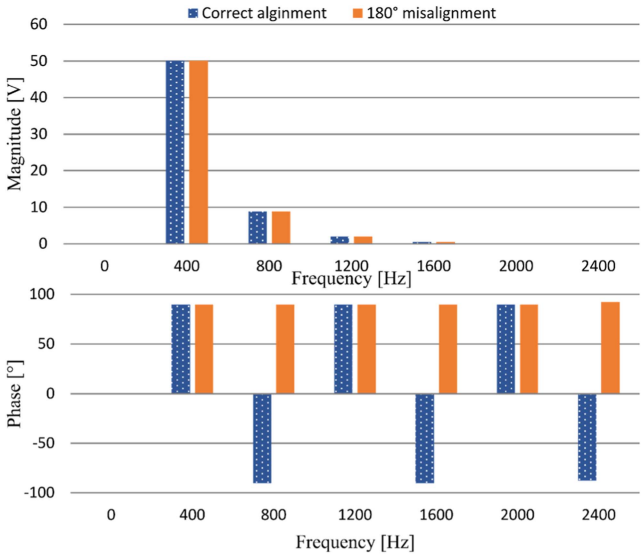


Fig. 13. Harmonic content when applying an FFT to the skewed voltage waveforms of Fig. 12(b). Example: Magnitude = 50 V, Frequency: 400 Hz, Phase = 90° → 50 cos((2πt) · 400 + π/2).

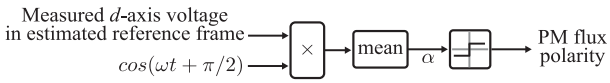


Fig. 14. Block diagram of simple proposed method to extract the PM flux polarity information without the need for an FFT.

voltages instead of currents. However, the difference in the positive and negative peaks of the voltage is minimal, as seen in Fig. 12(b), making it almost impractical to achieve polarity identification via this method. Nevertheless, the machine terminal voltage waveform is skewed due to the magnetic saturation, as seen in Fig. 12(b), where the skew direction is dependent on the PM flux's polarity.

Fig. 13 shows the results of applying an FFT to the skewed voltage waveforms of Fig. 12(b). Notice that these waveforms have the strong presence of a second harmonic (800 Hz). Moreover, the even harmonics phase depends on the skew direction or, in other words, on the PM flux polarity. Notice that, for the correct alignment of the PM, the phase of the even harmonics is $-90°$. On the other hand, for the misaligned case, the phase of the even harmonics is $+90°$ or in phase with the fundamental. Therefore, even harmonic phases can discriminate the PM flux polarity.

Fig. 14 shows the control block diagram of a simple proposed method to extract the PM flux polarity information from the second harmonic, the largest one, without needing an FFT, minimizing the computational burden of the proposed PM flux direction identification method. The mathematical implication of the proposed method in Fig. 14 is shown in

$$\alpha = \frac{1}{T_h}\int_0^{T_h} v_d^{\hat{e}} \cos\left(2\omega_h t + \frac{\pi}{2}\right) dt$$

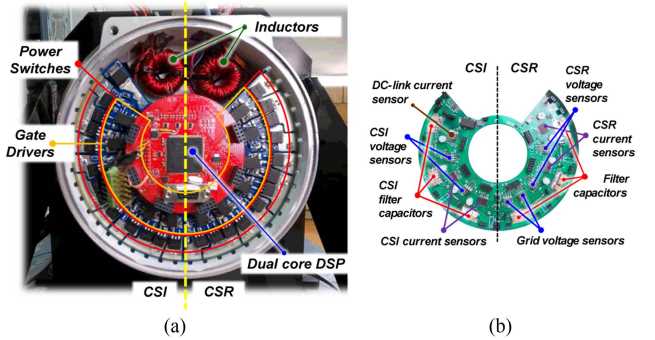


(a) (b)

Fig. 15. Fully-assembled CSI-IMD and its components. (a) Fully assembled demonstrator with endcap removed. (b) Endcap with 3 W integrated cooling fan. (c) Sensor board. (d) Power board. (e) Controller board. (f) DC-link inductors. (g) Incremental encoder.

$$\begin{aligned}\alpha &= \frac{1}{T_h}\int_0^{T_h} (v_1\cos(\omega_h t + \phi_1) + v_2\cos(2\omega_h t + \phi_2) \\ &\quad + v_3\cos(3\omega_h t + \phi_3) + \cdots)\cos\left(2\omega_h t + \frac{\pi}{2}\right) dt \\ \alpha &= \frac{1}{T_h}\int_0^{T_h} v_2\cos(2\omega_h t + \phi_2)\cos\left(2\omega_h t + \frac{\pi}{2}\right) dt \\ \alpha &= \frac{v_2}{2}\cos\left(\phi_2 - \frac{\pi}{2}\right). \end{aligned} \quad (15)$$

In (15), $v_d^{\hat{e}}$ is the measured $d$-axis voltage in the estimated reference frame composed of multiple harmonics components, as highlighted in Fig. 12. The measured $d$-axis voltage $v_d^{\hat{e}}$ is multiplied by $\cos(2\omega_h t + \frac{\pi}{2})$ and later integrated over a full period of the high frequency fundamental component $T_h = \frac{1}{f_h}$. It is known that the integral (over a full period) of terms originated from the multiplication of two components of different frequencies is always zero. Thus, the only term left after applying the integral is $\frac{T_h v_2}{2}\cos(\phi_2 - \frac{\pi}{2})$, and its value depends on the phase of the second harmonic of $v_d^{\hat{e}}$. As seen in Fig. 13, the phase of the second harmonic is $-90°$ for the correct alignment of the PM flux and 90° for the reversed alignment. Therefore, the term $\alpha = \frac{v_2}{2}\cos(\phi_2 - \frac{\pi}{2})$ is equal to $-\frac{v_2}{2}$ in case of correct alignment and $\frac{v_2}{2}$ in case of reversed alignment. Notice that this method (i.e., Fig. 14 and (15)) is insensitive to sensors' offset since the measured voltage is multiplied by a cosine function $\cos(2\omega_h t + \frac{\pi}{2})$ before being integrated. In fact, this method is only sensitive to noises of a frequency component of $2\omega_h$.

## VI. Experimental Verification

This section presents experimental results for the analysis above. The experiments were conducted using a 3 kW CSI integrated motor drive (IMD). Fig. 15 presents the assembled 3 kW CSI-IMD and its constituent parts. The system consists of a current source rectifier and a CSI arranged in a back-to-back configuration, as depicted in the power and sensor boards. The controller TMS320F28379D is used to generate the gate signals and to implement the inverter control algorithm. It is important to mention that a data-logging capability was implemented in the controller, allowing to collect simultaneously the estimated

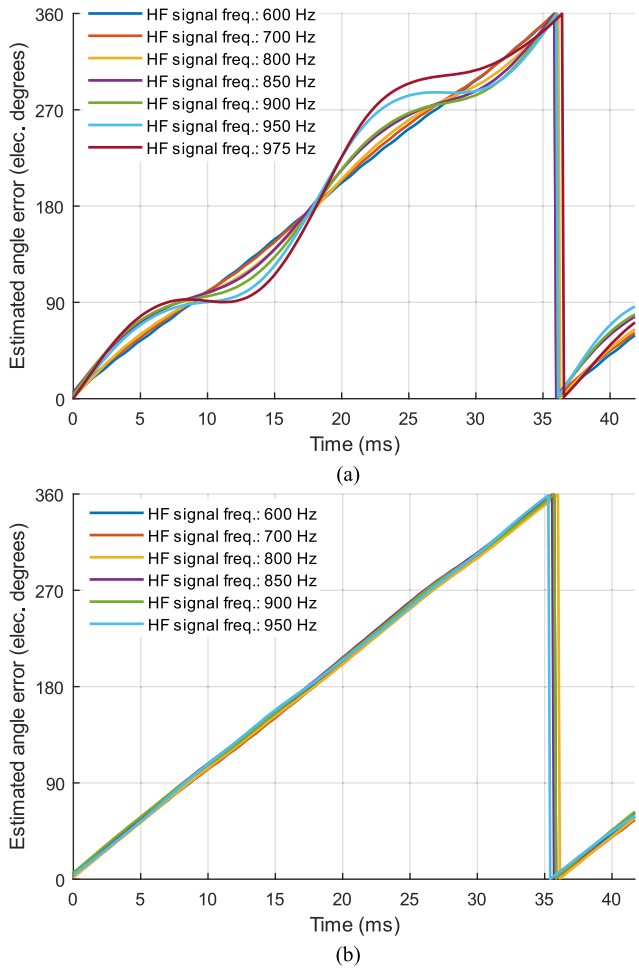


Fig. 16. Measured rotor position estimates using the PVE method under two different conditions. (a) Unbalanced output capacitors ($C_a = 1.1 \cdot 2.2\ \mu$F, $C_b = 2.2\ \mu$F, $C_c = 0.9 \cdot 2.2\ \mu$F). (b) Balanced output capacitors ($C_a = C_b = C_c = 2.2\ \mu$F) at 26.66 Hz fundamental electrical frequency (400 r/min). The frequency of the high-frequency injected signal is varied from 600 Hz to 975 Hz.

rotor position and the actual rotor position measured from a 12-bit incremental encoder at the sampling rate of 70 kHz (same rate as the control loop).

### A. Experimental Verification of Unbalanced CSI Output Capacitor's Impact on PVE's Performance

Fig. 16(a) and (b) compares the measured rotor position estimation using the PVE method for two different conditions: 1) unbalanced output capacitors ($C_a = 1.1 \cdot 2.2\ \mu$F, $C_b = 2.2\ \mu$F, $C_c = 0.9 \cdot 2.2\ \mu$F); and 2) balanced output capacitors ($C_a = C_b = C_c = 2.2\ \mu$F). Notably, the capacitor imbalance in condition 1) was intentionally created by adding or removing parallel capacitors. The capacitance ratios of 1.1 and 0.9 were verified by measuring the capacitance of each phase. For both conditions, the frequency of the HF injected signal was varied from 600 Hz to 975 Hz, and the fundamental electrical frequency was held constant at 26.66 Hz, the same excitation frequency used for the simulation results in Fig. 10. Comparing Fig. 16(a) and (b) shows that unbalanced CSI output capacitors substantially degrade the performance of the PVE rotor position estimation, when the frequency of the injected signal is close to the resonant frequency. This result is consistent with the trends exhibited by the analytical results in previous sections. The rotor position estimation waveforms of Fig. 16(a) reflect the same angle-dependent behavior shown in Fig. 10, where the capacitor unbalance creates an oscillatory error with a frequency two times the fundamental excitation frequency. The experimental results in Fig. 16(a) also confirm that the effects of the output capacitor unbalance become more prominent as the injection frequency increases.

The parameters and test conditions used for the simulation results in Fig. 10 were set to match those of the experimental results presented in Fig. 16(a) as closely as possible. However, the instability threshold of the PVE algorithm was reached during the experimental tests at a HFI frequency of approximately 1000 Hz, which is lower than the 1300 Hz threshold frequency predicted by the simulation results. This difference could be caused by various factors, including parameter errors in the simulation, additional noise in the experiments, or higher unbalance in the capacitor values than expected. This last factor is a plausible contributor since the tolerance range of the capacitor values that were used during the experiments (KRM55TR73A224MH01K) is 20%.

### B. Experimental Verification of Proposed PM Flux's Polarity Identification Method

The experimental results presented here were conducted using the CSI-fed SPM motor drive with parameters presented in Table I.

To experimentally verify the proposed PM flux polarity identification method, the algorithm in Fig. 14 was implemented. However, instead of applying the average across a single cycle of the HF injected signal, the average was used over 2000 cycles to improve the SNR. The proposed strategy should be verified for any rotor position; therefore, the experiment was conducted for a full 360° electrical rotation in steps of 15°. Again, two conditions were evaluated: 1) the estimated reference frame is correctly aligned with the PM flux, and 2) the estimated reference frame is 180° misaligned. Fig. 17 shows the experimental results obtained. In Fig. 17, the solid lines correspond to the data collected when the estimated reference frame is 180° misaligned (after the convergence of the HFI rotor position estimation method), and the dashed lines correspond to a correct alignment. Additionally, the test is conducted for three current amplitudes of the injected HF signal: 1 A, 2 A, and 3 A.

Fig. 17 demonstrates that, by looking at the $\alpha$ value [described in (15)], the PM flux polarity can be identified, where positive values of $\alpha$ indicate that the estimated reference frame $d$-axis is 180° misaligned, and negative values indicate correct alignment. Note that the value of $\alpha$ can vary for different rotor positions, suggesting that the effect of the saturation is more pronounced at some rotor positions than others. When injecting current values lower than approximately 1 A, the saturation effect can be sufficiently low at some rotor positions that the method fails

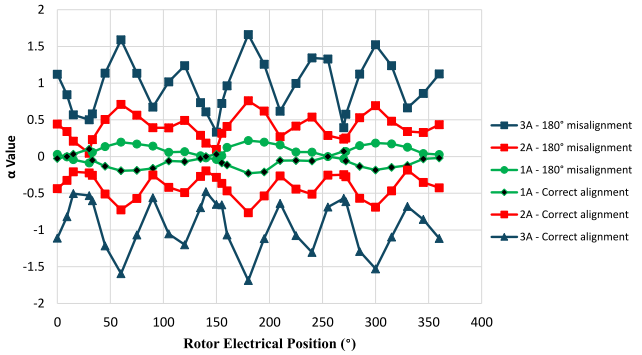


Fig. 17. $\alpha$ value used for the PM flux polarity identification using proposed method.

due to minor measurement errors. This can be observed by noticing that the solid blue line becomes negative, and the dashed black line becomes positive for some rotor position angles. Nevertheless, increasing the injected HF current intensifies the saturation effect, and the PM polarity can be safely determined, as shown by the green and red lines corresponding to 2 A and 3 A, respectively. Notice that the motor used in the experiment can withstand a maximum continuous current of up to 21.2 Arms.

## VII. Conclusion

This article has investigated the issue of tailoring PVE for rotor position estimation of SPM machines using CSI-based motor drives at static and low-speed operation. A detailed mathematical model for the rotor position estimation method has been developed, providing the analytical platform needed to investigate key implementation issues, including the impact of capacitor unbalance and CSI-load resonance.

The article has shown that CSIs using WBG switches can provide an appealing environment for implementing self-sensing of rotor angular position based on HF signal injection techniques using PVE. This investigation has revealed that the output filter capacitors of the CSI provide both opportunities and challenges for PVE. First, the resonance circuit created by the output filter capacitance and the machine inductance can be used to amplify the HF-injected signal, improving the SNR. On the other hand, injecting the HF signal close to the resonant frequency makes the rotor position estimation more sensitive to unbalanced output capacitor values.

A combination of analytical and experimental results has confirmed the importance of making a special effort to ensure that the filter capacitors are well-balanced; if not, the performance of the rotor position estimator of PVE can be seriously degraded, introducing severe errors in the angle estimates at two times the fundamental frequency.

The frequency of the injected signal can also play an essential role in determining the performance of the position estimator of the PVE. The frequency provides the freedom to adjust its value dynamically during operation, providing opportunities for optimizing its value that extend beyond the scope of this article. More of these particularities related to extracting maximum performance from self-sensing rotor position estimation techniques in CSI-based motor drives will be addressed in future publications, such as transitioning strategies between back-EMF and HFI methods (i.e., the transition from low-speed to high-speed operation).

In addition, this article proposes a PM flux polarity identification method for a CSI-fed SPM machine drive. This method is essential in the initial rotor position estimation using PVE. Instead of using peak values of the measured response to the injected HF signal (typical in VSI-fed PM motor drives), the proposed method uses the phase of the measured voltage signal's second-order harmonic. A practical algorithm without a fast Fourier transform is proposed to implement the proposed PM flux polarity identification method online. The proposed method's effectiveness is experimentally verified.

## Appendix

This appendix performs transformations between different coordinate systems to analyze the impedances of an unbalanced three-phase capacitive filter and an electric machine. The final overall impedance matrix in the *dq*-frame is then computed, with a specific interest in the OFF-diagonal element $Z_{dqh}$. Equation (A.1) shows the capacitive filter admittance matrix in the *abc* frame, where each term of the matrix can be calculated based on the (A.2)

$$\underline{\mathbf{Y}_{C_{abc}}} = \begin{bmatrix} \boldsymbol{Y}_{C\,aa} & \boldsymbol{Y}_{C\,ab} & \boldsymbol{Y}_{C\,ca} \\ \boldsymbol{Y}_{C_{ab}} & \boldsymbol{Y}_{C\,bb} & \boldsymbol{Y}_{C\,bc} \\ \boldsymbol{Y}_{C_{ca}} & \boldsymbol{Y}_{C_{bc}} & \boldsymbol{Y}_{C\,cc} \end{bmatrix} \tag{A.1}$$

$$\begin{aligned}
\boldsymbol{Y}_{C_{aa}} &= \frac{\boldsymbol{Z}c_b + \boldsymbol{Z}c_c}{\boldsymbol{Z}c_a\left(\boldsymbol{Z}c_b + \boldsymbol{Z}c_c\right) + \left(\boldsymbol{Z}c_b\boldsymbol{Z}c_c\right)} \\
\boldsymbol{Y}_{C_{bb}} &= \frac{\boldsymbol{Z}c_a + \boldsymbol{Z}c_c}{\boldsymbol{Z}c_b\left(\boldsymbol{Z}c_a + \boldsymbol{Z}c_c\right) + \left(\boldsymbol{Z}c_a\boldsymbol{Z}c_c\right)} \\
\boldsymbol{Y}_{C_{cc}} &= \frac{\boldsymbol{Z}c_b + \boldsymbol{Z}c_a}{\boldsymbol{Z}c_c\left(\boldsymbol{Z}c_b + \boldsymbol{Z}c_a\right) + \left(\boldsymbol{Z}c_b\boldsymbol{Z}c_a\right)} \\
\boldsymbol{Y}_{C_{ab}} &= -\frac{\boldsymbol{Z}c_c}{\left(\boldsymbol{Z}c_a + \boldsymbol{Z}c_c\right)\boldsymbol{Z}c_b + \boldsymbol{Z}c_a\boldsymbol{Z}c_c} \\
\boldsymbol{Y}_{C_{bc}} &= -\frac{\boldsymbol{Z}c_a}{\left(\boldsymbol{Z}c_b + \boldsymbol{Z}c_a\right)\boldsymbol{Z}c_c + \boldsymbol{Z}c_b\boldsymbol{Z}c_a} \\
\boldsymbol{Y}_{C_{ca}} &= -\frac{\boldsymbol{Z}c_b}{\left(\boldsymbol{Z}c_c + \boldsymbol{Z}c_b\right)\boldsymbol{Z}c_a + \boldsymbol{Z}c_c\boldsymbol{Z}c_b}
\end{aligned} \tag{A.2}$$

where $\boldsymbol{Z}c_x = \frac{1}{j\omega_h C_x}$, $x \to a, b, c$.

The capacitive filter admittance matrix can be transformed to the stationary *dq* reference frame using the Clarke-Park and inverse Clarke-Park transformation matrices, as shown in (A-3) $\underline{\mathbf{Y}_{\mathrm{Cdq}}} = \underline{CP} \cdot \underline{\mathbf{Y}_{C_{abc}}} \cdot \underline{CP^{-1}}$, where

$$\underline{CP} = \frac{2}{3}\begin{bmatrix} \cos(\theta_r) & \cos\left(\theta_r - \frac{2\pi}{3}\right) & \cos\left(\theta_r + \frac{2\pi}{3}\right) \\ -\sin(\theta_r) & -\sin\left(\theta_r - \frac{2\pi}{3}\right) & -\sin\left(\theta_r + \frac{2\pi}{3}\right) \end{bmatrix}$$

$$\underline{CP^{-1}} = \begin{bmatrix} \cos(\theta_r) & -\sin(\theta_r) \\ \cos\left(\theta_r - \frac{2\pi}{3}\right) & -\sin\left(\theta_r - \frac{2\pi}{3}\right) \\ \cos\left(\theta_r + \frac{2\pi}{3}\right) & -\sin\left(\theta_r + \frac{2\pi}{3}\right) \end{bmatrix}. \tag{A.3}$$

The $dq$-axis capacitive filter admittance matrix can, then, be combined with the machine $dq$-axis admittance matrix, as shown in (A.4), to obtain the overall admittance. Finally, the overall impedance matrix in the $dq$ frame is calculated by inverting the $dq$ -axis admittance matrix, as shown in (A.5)

$\underline{\mathbf{Y}_{\text{dqh}}} = \underline{\mathbf{Y}_{C_{dq}}} + \underline{\mathbf{Y}_{m_{dq}}}$, where

$$\underline{\mathbf{Y}_{m_{dq}}} = \begin{bmatrix} \boldsymbol{Z}_{m_d} & \boldsymbol{Z}_{m\,dq} \\ \boldsymbol{Z}_{m\,dq} & \boldsymbol{Z}_{m_q} \end{bmatrix} \tag{A.4}$$

$$\boldsymbol{Z}_{m_d} \approx\ j\omega_h L_d,\ \boldsymbol{Z}_{m_q} \approx j\omega_h L_q, \text{ and } \boldsymbol{Z}_{m_{dq}} \approx 0$$

$$\underline{\boldsymbol{Z}_{\text{dqh}}} \triangleq \begin{bmatrix} \boldsymbol{Z}_{dh} & \boldsymbol{Z}_{dqh} \\ \boldsymbol{Z}_{dqh} & \boldsymbol{Z}_{qh} \end{bmatrix} = \underline{\mathbf{Y}_{\text{dqh}}}^{-1}. \tag{A.5}$$

## ACKNOWLEDGMENT

The views and opinions of authors expressed herein do not necessarily state or reflect those of the United States Government or any agency thereof.

## REFERENCES

[1] R. A. Torres, H. Dai, W. Lee, T. M. Jahns, and B. Sarlioglu, "Evaluation of sensorless techniques for surface permanent-magnet integrated motor drive using current-source inverter," in *Proc. IEEE Energy Convers. Congr. Expo.*, 2020, pp. 2387–2394.

[2] S. Bolognani, L. Tubiana, and M. Zigliotto, "Extended kalman filter tuning in sensorless PMSM drives," *IEEE Trans. Ind. Appl.*, vol. 39, no. 6, pp. 1741–1747, Nov. 2003.

[3] J.-H. Jang, S.-K. Sul, J.-I. Ha, K. Ide, and M. Sawamura, "Sensorless drive of surface-mounted permanent-magnet motor by high-frequency signal injection based on magnetic saliency," *IEEE Trans. Ind. Appl.*, vol. 39, no. 4, pp. 1031–1039, Jul. 2003.

[4] B. J. Baliga et al., "The BiDFET device and its impact on converters," *IEEE Power Electron. Mag.*, vol. 10, no. 1, pp. 20–27, Mar. 2023, doi: 10.1109/MPEL.2023.3237059.

[5] V. Madonna, G. Migliazza, P. Giangrande, E. Lorenzani, G. Buticchi, and M. Galea, "The rebirth of the current source inverter: Advantages for aerospace motor design," *IEEE Ind. Electron. Mag.*, vol. 13, no. 4, pp. 65–76, Dec. 2019, doi: 10.1109/MIE.2019.2936319.

[6] X. Fan, D. Li, W. Kong, L. Cao, R. Qu, and Z. Yin, "Fast calculation of strand eddy current loss in inverter-fed electrical machines," *IEEE Trans. Ind. Electron.*, vol. 70, no. 5, pp. 4640–4650, May 2023.

[7] S. Woolaghan and N. Schofield, "Current source inverters for PM machine control," in *Proc. IEEE Int. Electric Machines Drives Conf.*, Miami, FL, USA, 2009, pp. 702–708.

[8] J.-H. Song, K.-B. Kim, and M.-J. Youn, "Eigenvalue sensitivity of a speed-sensorless CSI-fed induction motor system," in *Proc. 19th Annu. Conf. IEEE Ind. Electron.*, 1993, pp. 987–991.

[9] J. Hu and B. Wu, "Field oriented control CSI synchronous motor drive without shaft sensors," in *Proc. Int. Conf. Power Electron. Drive Syst.*, 1997, vol. 2, pp. 798–803.

[10] H. Feroura, F. Krim, B. Talbi, A. Laib, and A. Belaout, "Sensorless field oriented control of current source inverter fed induction motor drive," *Revue Roumaine des Sci. Techniques, Série Électrotechnique et Énergétique*, vol. 63, no. 1, pp. 100–105, 2018.

[11] Q. Song, Z. Wang, P. Liu, Y. Xu, C. Tang, and M. Cheng, "Sensorless control of current-source-converters fed synchronous motor drives using high frequency signal injection," in *Proc. Int. Conf. Elect. Machines Syst.*, 2019, pp. 1–5.

[12] M. Morawiec and F. Wilczynski, "Sensorless control of five-phase machine supplied by the current source inverter," in *Proc. Int. Conf. Elect. Power Drive Syst.*, 2020, pp. 1–6.

[13] A. Nikolic and B. Jeftenic, "Speed sensorless direct torque control implementation in a current source inverter fed induction motor drive," in *Proc. IEEE 35th Annu. Power Electron. Specialists Conf.*, 2004, pp. 2843–2848.

[14] M. Meiqin, L. Fuyan, M. Junsheng, and X. Bin, "Sensorless control of PMSG for a wind power system based on CSC," in *Proc. 8th Int. Conf. Power Electron.*, 2011, no. 1, pp. 2175–2179.

[15] Z. Wang, Y. Zheng, Z. Zou, and M. Cheng, "Position sensorless control of interleaved CSI fed PMSM drive with extended kalman filter," *IEEE Trans. Magn.*, vol. 48, no. 11, pp. 3688–3691, Nov. 2012.

[16] A. K. Abdelsalam, M. I. Masoud, M. S. Hamad, and B. W. Williams, "Improved sensorless operation of a CSI-based induction motor drive: Long feeder case," *IEEE Trans. Power Electron.*, vol. 28, no. 8, pp. 4001–4012, Aug. 2013.

[17] E. Al-nabi, B. Wu, N. R. Zargari, and V. Sood, "Sensorless control of CSC-fed IPM machine for zero- and low-speed operations using pulsating HFI method," *IEEE Trans. Ind. Electron.*, vol. 60, no. 5, pp. 1711–1723, May 2013.

[18] H. C. Chen and H. H. Huang, "Design of buck-type current source inverter fed brushless DC motor drive and its application to position sensorless control with square-wave current," *IET Electr. Power Appl.*, vol. 7, no. 5, pp. 416–426, 2013.

[19] P. D. Jyothsna and S. Harinath, "Sensor-less operation of CSI fed induction motor drive by using MRAS," *IOSR J. Electr. Electron. Eng.*, vol. 9, no. 6, pp. 1–6, 2014.

[20] M. Morawiec, "Sensorless control of induction machine supplied by current source inverter," *Asian J. Control*, vol. 17, no. 6, pp. 2403–2408, Nov. 2015.

[21] E. Al-nabi, "Sensorless current source-fed PM drive system for low speed operations," Toronto Metrop. Univ., Jan. 1, 2013, doi: 10.32920/ryerson.14664582.v1.

[22] R. A. Torres, H. Dai, W. Lee, T. M. Jahns, and B. Sarlioglu, "A simple and robust controller design for high-frequency WBG-based current-source-inverter-fed AC motor drive," in *Proc. IEEE Transp. Electrific. Conf. Expo*, Chicago, IL, USA, 2020, pp. 111–117.

[23] Y. Li, Z. Q. Zhu, D. Howe, C. M. Bingham, and D. A. Stone, "Improved rotor-position estimation by signal injection in brushless AC motors, accounting for cross-coupling magnetic saturation," *IEEE Trans. Ind. Appl.*, vol. 45, no. 5, pp. 1843–1850, Sep./Oct. 2009.

[24] R. A. Torres, H. Dai, W. Lee, B. Sarlioglu, and T. Jahns, "Current-source inverter integrated motor drives using dual-gate four-quadrant wide-bandgap power switches," *IEEE Trans. Ind. Appl.*, vol. 57, no. 5, pp. 5183–5198, Sep./Oct. 2021.

[25] S. Kondo, A. Takahashi, and T. Nishida, "Armature current locus based estimation method of rotor position of permanent magnet synchronous motor without mechanical sensor," in *Proc. IEEE Ind. Appl. Conf. 30th IAS Annu. Meeting*, 1995, vol. 1, pp. 55–60.

**Renato Amorim Torres** (Member, IEEE) received the B.Sc. degree from the Federal University of Minas Gerais, Belo Horizonte, Brazil, in 2016, and the M.S. and Ph.D. degrees from the University of Wisconsin–Madison, Madison, WI, USA, in 2020 and 2022, respectively, all in electrical engineering.

During his M.S. and Ph.D. studies, he was a Research Assistant with the Wisconsin Electric Machines and Power Electronics Consortium. Since completing his Ph.D., he was a Researcher in Electric Machines and Drive Systems at General Motors Research and Development.

**Sangwhee Lee** (Member, IEEE) received the B.S. degree in electrical engineering from the Korea University, Seoul, South Korea, in 2018 and the M.S. and Ph.D. degrees in electrical and computer engineering from the University of Wisconsin-Madison, Madison, WI, USA, in 2020 and 2024, respectively.

He has been a Research Assistant with the Wisconsin Electric Machines and Power Electronics Consortium since 2019. His research interests include power electronics and their advanced controls, PWM, transportation electrification, grid modernization with renewable integration, and electromagnetic interference.

Mr. Lee was a recipient of two IEEE student competition awards and the Novotny Power Engineering Award from the University of Wisconsin-Madison in 2023.

**Hang Dai** (Member, IEEE) received the B.Eng. degree from North China Electric Power University, Beijing, China, in 2015, and the Ph.D. degree from the University of Wisconsin-Madison, Madison, WI, USA, in 2021, all in electrical engineering.

His research interests include power electronics and energy conversion systems.

**Woongkul Lee** (Member, IEEE) received the B.S. degree in electrical and electronic engineering from Yonsei University, Seoul, South Korea, in 2013, and the M.S. and Ph.D. degrees in electrical engineering from the University of Wisconsin-Madison, WI, USA, in 2016 and 2019, respectively.

He was a Postdoctoral Research Associate with the Wisconsin Electric Machines and Power Electronics Consortium, University of Wisconsin-Madison from 2019 to 2020. In 2024, he was with Elmore Family School of Electrical and Computer Engineering, Purdue University as an Assistant Professor. Prior to that, he was an Assistant Professor with Michigan State University. His research interests include high-performance motor drive, power electronics, electric machines, and distributed energy resources.

**Thomas M. Jahns** (Life Fellow, IEEE) received the S.B., S.M., and Ph.D. degrees in electrical engineering from the Massachusetts Institute of Technology, Cambridge, MA, USA, in 1974 and 1978, respectively.

In 1998, he was with the Department of Electrical and Computer Engineering, University of Wisconsin-Madison, as a Grainger Professor of Power Electronics and Electric Machines, where he was Co-Director/Director with the Wisconsin Electric Machines and Power Electronics Consortium for 14 years from 2007 to 2021. Prior to joining UW, he was with GE Corporate Research and Development (now GE Global Research Center), Niskayuna, NY, USA, for 15 years. From 1996 to 1998, he conducted a research sabbatical at MIT, where he directed research activities in the area of advanced automotive electrical systems as Co-Director of an industry-sponsored consortium. Following his retirement from the active faculty in 2021, he is continuing to pursue research as a Grainger Emeritus Professor in the areas of high-performance permanent magnet synchronous machine drives using wide-bandgap power switches, and integrated motor drives using modular topologies to achieve high fault tolerance.

Dr. Jahns was the recipient of the 2005 IEEE Nikola Tesla Technical Field Award and the IAS Outstanding Achievement Award in 2011. He was both the IEEE Industry Applications Society and Power Electronics Society (PELS) as a Distinguished Lecturer. He is a Past President of PELS and served two years as Division II Director on the IEEE Board of Directors (2001/2002). He was elected as a member of the US National Academy of Engineering in 2015 and selected as the recipient of the 2022 IEEE Medal in Power Engineering.

**Bulent Sarlioglu** (Fellow, IEEE) received the B.S. degree from Istanbul Technical University, Istanbul, Turkey, in 1990, the master's degree from the University of Missouri, Columbia, MO, USA, in 1992, and the Ph.D. degree from the University of Wisconsin–Madison, Madison, WI, USA, in 1999, all in electrical engineering.

Since 2011, he has been a Professor with the University of Wisconsin–Madison and an Associate Director of the Wisconsin Electric Machines and Power Electronics Consortium. From 2000 to 2011, he was with the Aerospace Division, Honeywell International Inc., Torrance, CA, USA, most recently as a Staff Systems Engineer. He is the Inventor or Coinventor of 24 U.S. and many international patents. He has more than 280 technical papers published in conference proceedings and journals. His research interssts include electrical machines, drives, and power electronics.

Dr. Sarlioglu was a recipient of the Honeywell's Outstanding Engineer Award in 2011, the NSF CAREER Award in 2016, the 4th Grand Nagamori Award from Nagamori Foundation, Japan, in 2018, and the IEEE Power and Energy Society Cyril Veinott Electromechanical Energy Conversion Award in 2021. He was a Distinguished Lecturer for IEEE Industry Applications Society from 2019 to 2021. He is a Distinguished Lecturer for the IEEE Vehicular Technology Society. He was with many IEEE conferences, including the General Chair for IEEE Transportation Electrification Conference and Expo 2018 and the Technical Program Co-Chair for Energy Conversion Congress and Exposition 2019. He was elected as a Fellow of the National Academy of Inventors in 2021.